Gradients in solid surface tension drive Marangoni-like motions in cell aggregates

Vikrant Yadav, Md. Sulaiman Yousafzai, Sorosh Amiri, Robert W. Style, Eric R. Dufresne, and Michael Murrell

Phys. Rev. Fluids **7**, L031101 — Published 21 March 2022

DOI: 10.1103/PhysRevFluids.7.L031101

Gradients in Solid Surface Tension Drive Marangoni-like Motions in Cell Aggregates

V. Yadav[1,2],* M.S. Yousafzai[1,2,5],* S. Amiri[2,3], R. W. Style[4], E. R. Dufresne[4], and M. Murrell[1,2,4,5†]
[1]*Department of Biomedical Engineering, Yale University, 55 Prospect Street, New Haven, Connecticut 06511, USA*
[2]*Systems Biology Institute, Yale University, 850 West Campus Drive, West Haven, Connecticut 06516, USA*
[3]*Department of Mechanical Engineering and Material Science, Yale University, 10 Hillhouse Avenue, New Haven, Connecticut 06511, USA*
[4]*Department of Materials, ETH Zurich, Zurich 8093, Switzerland and*
[5]*Department of Physics, Yale University, 217 Prospect Street, New Haven, Connecticut 06511, USA*
(Dated: March 3, 2022)

The surface tension of living cells and tissues originates from the generation of non-equilibrium active stresses within the cell cytoskeleton. Here, using laser ablation, we generate gradients in the surface tension of cellular aggregates as models of simple tissues. These gradients of active surface stress drive large-scale and rapid toroidal motion. Subsequently, the motions spontaneously reverse as stresses re-accumulate and cells return to their original positions. Both forward and reverse motions resemble Marangoni flows in viscous fluids. However, the motions are faster than the timescales of viscoelastic relaxation and the surface tension gradient is proportional to mechanical strain at the surface. Further, due to active stress, both the surface tension gradient and surface strain are dependent upon the volume of the aggregate. These results indicate that surface tension can induce rapid and highly correlated elastic deformations in the maintenance of tissue shape and configuration.

Whenever there is a gradient in surface tension along an interface, there is an associated shear stress. For the interfaces of fluids, this results in a flow near the interface that converges on regions of high surface tension, known as the Marangoni effect [1]. One classic example is "tears of wine" [2]. Marangoni stresses are also well known to cause convection in thin, heated films, driven by local temperature gradients along the film surface, and arise whenever there are surfactant or solute gradients [3]. While Marangoni effects have been studied extensively in simple fluids, and to some extent in viscoelastic fluids [4–6], their impact on solids appears to be unexplored. In part, this is because surface tension driven deformations of solids are *typically* limited to lengthscales smaller than the elastocapillary length $l = \gamma/E$ (where γ is the surface tension and E is Young's modulus) [7]. However, in living systems, the magnitude of stresses caused by cell and tissue surface tensions may be comparable to their bulk elasticity on cellular lengthscales [8, 9]. Thus, capillary effects may play a large role in their mechanical behaviors.

Tissue surface tension originates in the non-equilibrium activity of mechano-chemical enzymes within the cell cytoskeleton that convert chemical energy into "active" stress [10–12]. At the cellular level, these stresses contribute to cortical and membrane tensions that determine cell shape and mediate their response to mechanical perturbation [13–17]. At large scales, cortical tensions are coupled together *via* cell-cell adhesions and lead to tissue surface tensions [16, 18–20]. In the bulk of the tissue, stresses may lead to a heterogenous pressure profile, and reorganize the distribution of cells [21–25]. Tissue surface tension has been considered liquid-like on timescales of cell migration, in which the turnover of cell-cell adhesion relaxes internal stress [26]. On shorter timescales, the surface tension may be solid-like [27]. Likewise, the effects of gradients in solid surface tension may impact cell motion.

In this Letter, we show that surface tension gradients can drive rapid and large-scale collective motions within cellular aggregates, as models of simple tissues. We use laser ablation to quickly and locally reduce aggregate surface tension, creating shear stresses at the surface. This drives large-scale cell movements which reverse as surface tension re-accumulates. These motions include multiple timescales, which are compared to the viscoelastic relaxation timescale to determine the extent to which they can be considered elastic or viscous. To further make this determination, we measure the strain in the cells at the aggregate surface, and compare it to the estimated surface tension gradient to define an effective surface modulus. Finally, we inhibit the conversion of chemical energy into active stress by myosin II molecular motors, to understand the role of non-equilibrium processes in the aggregate mechanical response.

Cell aggregates are composed of S180 murine sarcoma cells, formed from suspension spinning, and are $50-150$ μm in diameter (Supplementary Materials, Supplementary Fig. 1) [28, 29]. E-cadherin interactions induce cell-cell adhesion, leading to round aggregates with a smooth surface (Fig 1A). To generate gradients in surface tension, we use a high energy laser ($\lambda = 337$ nm, 40 mW) to ablate cells within a point at the surface of the non-adhered cell aggregate (Fig 1A, Supplementary Video 1). As the laser is focused at a 0.6μm diameter area (20X objective, NA 0.8), the number of cells removed during ab-

* These authors contributed equally.
† michael.murrell@yale.edu

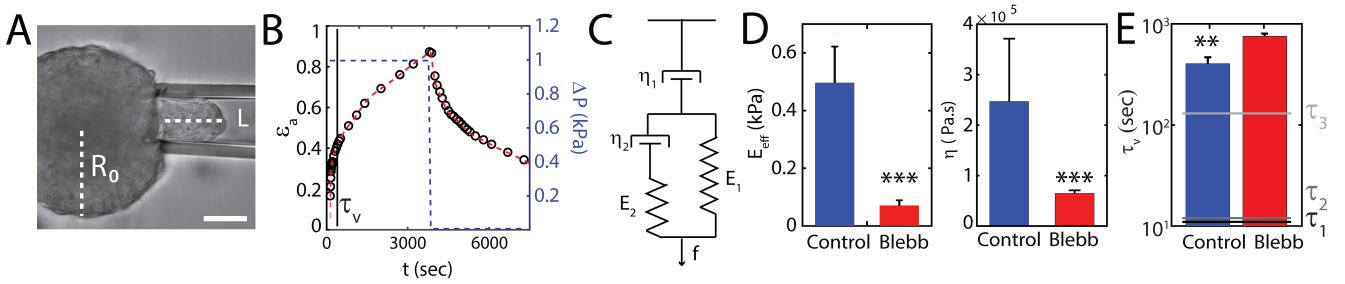

Figure 1. **Cell ablation at aggregate surface induces rapid, internal toroidal motions.** (A,left) DIC image of a cell aggregate immediately prior to ablation. Location of ablation is at the red asterisk. (A,right) Kymographs depicting material displacement around cell surface. The yellow dashed line indicate path over which kymographs are calculated. White dotted line indicates region over which PIV is applied. (B) PIV of cellular motion ($\vec{v}$) analyzed from DIC images, taken at two different time points. Time between frames is 1 sec. (C) Mean speed and net material transport over time. The timescales of relaxation and reversal are denoted by τ_1, τ_2, and τ_3. (D, left) Image of a cell aggregate and (D, right) corresponding kymographs with 50 μM Blebbistatin. (E) PIV of cellular displacements with 50 μM Blebbistatin. (F) Mean speed and net material transport for Blebbistatin treated aggregate. Scale bars are 30μm.

lation is few and consistent across different experiments. We quantified the resultant time-resolved displacements using Particle Image Velocimetry (PIV, Supplementary Note 1). Using PIV measurements, we experimentally measure the flow profiles, calculate the shear strains at the surface and use the strains to calculate gradients in surface tension.

Immediately upon ablation, the surface of the aggregate retracts from the ablation site (Fig 1B). The rearward surface motions are concomitant with immediate forward motions of the core (center). In combination, these motions yield toroidal patterns that resemble Marangoni flows in liquid droplets (Supplementary Fig. 2) [30, 31]. There are multiple timescales within the observed motions. The timescale of the initial relaxation is rapid ($\tau_1 = 10$ sec). Subsequently, the surface and bulk motions reverse. Thus, the toroid reverses its orientation over two times scales - first quickly ($\tau_2 = 40$ sec), and then slowly as the aggregate approaches its original configuration ($\tau_3 = 70$ sec) (Fig 1C). To estimate the extent of reversibility in motion, and how much the aggregate re-establishes its original configuration, we calculate the net material displacement through the center of aggregate. The net material transport can be approximated as $\int_0^t v(t')dt'$ where, v is the velocity of material motion at the center of aggregate. The net material displacement increases with forward motion and decreases with reversal, finally returning to zero, indicating the motion is reversible (Fig. 1C). Both forward and reverse motions are dependent upon active stress - as aggregates treated with 50μM Blebbistatin, which inhibits myosin II ATPase activity, show no coherent motion upon ablation (Fig 1D-F, Supplementary Video 2).

To compare the observed timescales of motion and reversal with the viscoelastic timescale of the aggregate, we quantify the mechanical properties of the aggregate with micropipette creep and stress relaxation tests (Fig 2A,B, Supplementary Video 3, Supplementary Note 2, Supplementary Fig. 3). Briefly, a micropipette of 30 μm radius is used to apply a suction pressure on the aggregate. This draws a length, L, of aggregate into the pipette, which increases over time until the pressure is released (here after approximately 60 minutes), at which point L decreases. The changes in L with time reflect the viscoelasticity of the aggregate. Following previous work [32], the aggregate can be well described by the modified Maxwell model (Fig 2C, Supplementary Figure 4,5).

$$\varepsilon_a = \frac{f}{\eta_1}t + \frac{f}{E_1}\left(1 - \frac{E_2}{E_1+E_2}e^{-\frac{E_1E_2}{\eta_2(E_1+E_2)}t}\right) \quad (1)$$

Here, f is the applied micropipette stress, the strain, ε is defined as L_t/R_0, where R_0 is the undeformed radius of the aggregate, and E_1, E_2, η_1 and η_2 are viscoelastic constants of the modified Maxwell model. We define a viscoelastic timescale, $\tau_v = \eta_2/E_{eff}$, where E_{eff} is given by $E_1E_2/(E_1+E_2)$. Thus, at short times ($t \ll \tau_v$), the aggregate behaves as an elastic solid. By contrast, at long times ($t \gg \tau_v$), the aggregate flows like a liquid with viscosity η_1(Supplementary Fig. 4, 5, Supplementary note 3). This is consistent with previous studies that cell aggregates behave as solids at short time scales, and as fluids at long time scales [33–38].

We estimate the values of associated material parameters and time scales by fitting aspiration and retraction curves to eqn. 1. We find that $E_1 = 700$ Pa, $E_2 = 1.7$ kPa and $\eta_1 = 2.5 \times 10^5$ Pa.sec and $\eta_2 = 2 \times 10^5$ Pa.sec . Finally, using these fitted values we get $\tau_v = 402$ sec +/- 65 sec. Further, like the timescales of motion, we find that the magnitude of all parameters are dependent on the myosin activity, as all are reduced on treatment with 50μM Blebbistatin [39] (Fig 2D). Thus in the presence of active stress, we note that the timescales of motion as described in Fig. 1, are all shorter than the viscoelastic timescale as measured by micropipette (Fig 2E). We therefore conclude that all motions within the aggregate bulk are predominantly elastic.

Given these bulk rheological parameters, we can infer the surface properties that drive motion from the anal-

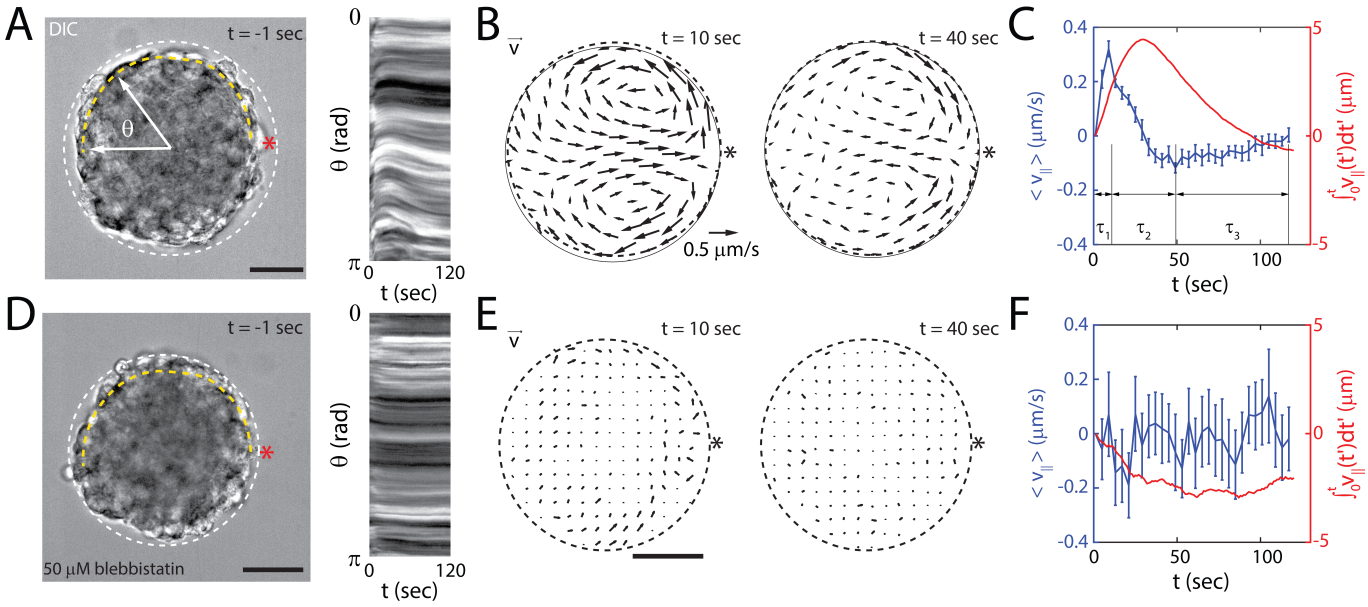

Figure 2. **The mechanical relaxation is slow compared to the timescales of motion.** (A) Brightfield image of an aggregate in the micropipette. (B) A step in pressure (ΔP) is applied to a cell aggregate of radius R_0 that brings the aggregate into the pipette, a length L and induces a strain, ε, as a function of time. The solid black line represents τ_v. (C) Modified Maxwell model applied to the evolution of ε with time. In the model, E_1 and E_2 are elastic modulus, and η_1 and η_2 are dashpots representing dissipative elements. f represents the stress applied to the system, in analogy to the applied pressure by micropipette. (D) The effective elastic modulus E_{eff}, and viscosity (η) obtained from fitting experimental data. (E) Viscoelastic relaxation time τ_v, of aggregates for an applied pressure of 1 kPa, in comparison with motion time scales τ_1, τ_2, and τ_3 as defined in Fig 1C (n = 10). Scale bar is 30 μm. *** $p < 0.001$, ** $p < 0.01$.

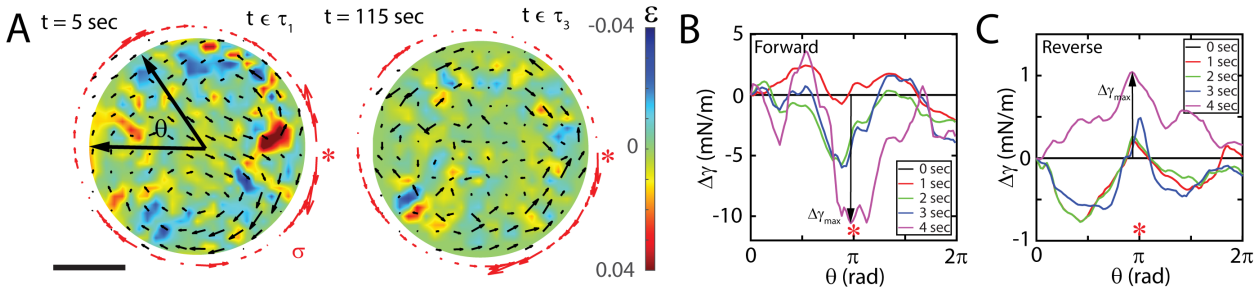

Figure 3. **Motions are driven by solid-like surface stresses.** (A) Cell displacement u (black vectors), areal strain field ($\varepsilon = \nabla \cdot u$) due to displacement (color map), and surface stresses (red vectors) associated with deformation at $t = 5$ sec (during τ_1) and $t = 115$ sec (during τ_3). (B) Change in surface tension in forward and (C) reverse motion, as a function of angular position θ, as measured from constitutive models. Asterisks indicates the region of ablation. Black arrow in B, and C denotes maximum change in surface tension at a given instant. Scale bar is 30 μm.

ysis of the deformations. For a single aggregate, both forward and reverse strains are measured by PIV (Fig 3A). For this, we calculate the displacements for $\Delta t =$ 4 sec in the forward direction ($t = 0$ sec to $t = 4$ sec, during τ_1), and for $\Delta t = 4$ sec in the reverse direction ($t = 120$ sec to $t = 116$ sec, during τ_3). This time interval is the longest time over which the vector field can be estimated using PIV for forward motion, and is used for the reverse motion for comparison. As $\Delta t \ll \tau_v$ (Fig 1C, 2E), we assume a linear elastic constitutive relationship, and multiply the strain by the modulus as measured by micropipette to estimate the surface stress. We use the shear stress measurements to calculate changes in surface tension along the aggregate periphery [40] (Supplementary Note 4, Supplementary Fig. 6). In particular, shear stresses at the surface, σ, must be balanced by a corresponding gradient in the surface tension, which is given by the following relation:

$$\sigma = G\varepsilon_s = d\gamma/ds = \frac{1}{R_0}\frac{d\gamma}{d\theta} \tag{2}$$

where ε_s is the shear strain, G is the shear modulus, s is

the arc-length along the aggregate surface, θ is the corresponding angular position, and R_0 is the radius of the aggregate. R_0, θ, and s are related by the constraint, $s = R_0\theta$. The calculation of shear strain, ε_s, from PIV data is outlined in Supplementary Note 4, and shear modulus, G is approximated as E_1. We integrate (2) with respect to θ to get changes in surface tension, $\Delta\gamma$, relative to a fixed starting point. Equation (2) assumes force balance at the aggregate surface, and does not require calculation of bulk stresses. The grid resolution used in PIV is 3.2 μm, which is comparable to the size of a cell. Therefore the calculated surface tensions pertain to a single cell layer at the surface of the aggregate. Relative to the initial time (forward motion), plots of $\Delta\gamma$ (Fig. 3B) show a localized drop in surface tension near the ablation point of 10 mN/m, which drives toroidal motion away from this point. Relative to the final time point (reverse motion) (Fig. 3C), over the same time interval, we see a localized increase of 1 mN/m, which pulls cells back in the opposite direction.

To understand the origin of the surface tension, we looked for changes to the cell morphology with aggregate size (volume). Specifically, we imaged the deformation of cell nuclei with a nuclei-localizing Green Fluorescence Protein (GFP, Fig. 4A). We observe that the nuclei closer to the edge of aggregate are significantly more elongated, whereas the ones closer to center are more rounded. The observed radial anisotropy is consistent with previous results [21, 41]. We quantify the extent that the nuclei are elongated compared to circular in shape, and define a strain $\varepsilon_N = AR - 1$, where AR is defined as the ratio of major and minor axis of an ellipse fitted on to the nuclei.

For aggregates of different sizes, we observe that the strain decreases monotonically with the size of the aggregate (Fig. 4B). Similarly, we quantify the surface tension difference $\Delta\gamma_{\max}$ during the initial retraction phase, τ_1. This represents the largest change in surface tension during the motion of the aggregate after ablation. Indeed, we observe that cellular aggregates demonstrate the presence of a size-dependent $\Delta\gamma_{\max}$ (Fig. 4C). The difference is largest for small aggregates, and decreases identically as strain for large aggregates.

We attribute the decrease in nuclear strain (ε_N) as well as the decrease in stress, to a decrease in density of phosphorylated myosin on the aggregate surface (Supplementary Fig. 7). Further, we find that like the phosphorylation of myosin, the strain, and the stress decreases monotonically with the size of the aggregate. Therefore, we suggest that there are strong active stresses at the surface although the existence of bulk stresses can not be excluded. However, suppression of motor activity by Blebbistatin suppresses all size-dependent effects (Fig 4B, Supplementary Fig. 7).

The co-variation of surface tension and nuclear strain with aggregate dimensions can be rationalized through a strain-dependent surface tension. Plotting $\Delta\gamma$ versus the surface strain, ε_N, which were independently plotted functions of aggregate size, R_0, we find a linear relationship between surface tension and nuclear strain (Fig. 4D). This slope of this surface constitutive relationship defines an apparent surface modulus, $E_s = 90\ mN/m$. This value is comparable to other soft solids, such as silicone gels [42–44] and cell membranes [45].

Intriguingly, the stress-strain curve extrapolates with a straight line to a non-zero $\Delta\gamma_{\max}$ at zero strain. We attribute this residual strain in the aggregate to the non-myosin-based components of surface tension (termed "passive" for simplicity) which are unperturbed by laser ablation. As Blebbistatin-treated aggregates do not flow after ablation, it is not possible to estimate surface stresses using the method described earlier. Therefore, passive contributions are not included in our estimate of $\Delta\gamma$. However, the aggregates retain a roughly spherical shape, indicative of passive surface stresses, likely emerging from cell-cell cohesion [46]. To provide additional evidence to the presence and magnitude of passive contributions to the surface tension, we measure the surface tension at long times by micropipette ($t \gg \tau_v$). In this case, we find that the surface tension for aggregates with active myosin is approximately 12.5 mN/m, in agreement with the surface tension gradient measured after ablation (Supplementary Figure 8). However, upon myosin inhibition, we find a surface tension of 4 mN/m. Thus, we suggest that passive contributions to the surface tension are approximately 30%.

The toroidal pattern of motion observed in our laser ablation experiments is a hallmark of Marangoni flows. However, there are several principal distinctions from traditional Marangoni flows.

First, the observed toroidal displacements are distinct from traditional Marangoni flows in that the timescales of motion are short compared to the characteristic viscoelastic timescale, suggesting they are elastic in nature. Further, the surface tension gradient that generates the displacement is strain-dependent, a hallmark of elastic solids. Thus, we conclude that the surface tension of aggregates on timescales on which toroidal motions are induced contain solid-like characteristics. While Marangoni flows are typically associated with surface tension-driven motion of fluids, the nature of the force balance remains the same for a linear elastic material. Indeed, one can be transformed to another by substituting the shear modulus with shear viscosity and displacements with velocities [47]. This equivalence between linear elasticity and the Stokes flow within the force balance indicates that surface tension gradients can equivalently drive Marangoni flows in fluids, or elastic Marangoni-like deformations in solids (Supplementary note 5).

Second, after the flows that relax the initial applied surface tension, as observed in passive droplets, the flows spontaneously reverse direction - a behavior unseen in passive systems. In doing so, aggregates in suspension return to their original shape and configuration. Elastic stresses that were relaxed are quickly re-accumulated using myosin-based active stresses. Thus, the aggregate may maintain “surface-tensional homeostasis” [48–

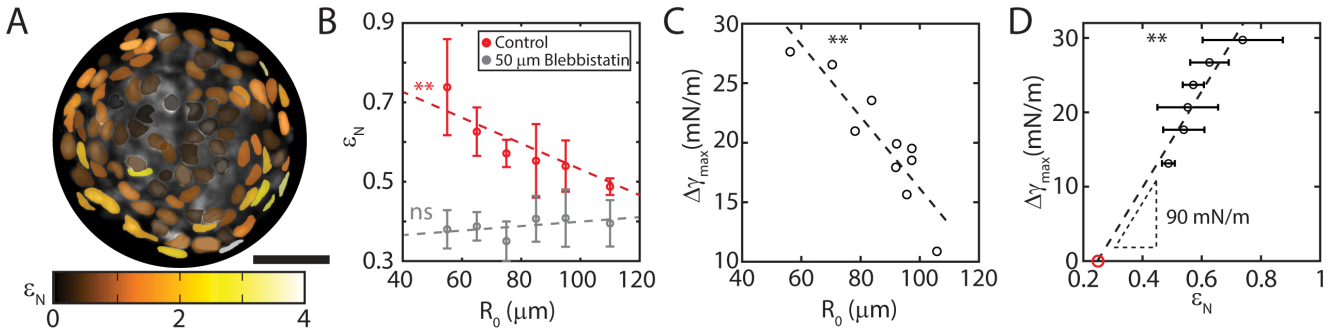

Figure 4. **Surface tensions are size-dependent and solid-like.** (A) Distribution of nuclear shapes inside an aggregate color coded by their strain defined as $\varepsilon_N = AR - 1$. Scale bar is 30 μm. (B) Average nuclear strain (n = 36) varies with the size of the aggregate, R_0.(C) Surface tension gradient, $\Delta\gamma$ (n = 10) varies with the size of the aggregate, R_0. (D) Surface tension gradient versus nuclear strain. Red dot indicates nuclear strain in the presence of 50 μM Blebbistatin. The slope of the curve represents the apparent surface modulus. ** $p < 0.01$, ns is non significant.

50], a principle by which the system desires to restore a set level of tension after perturbation, analogous to tensional homeostasis previously reported in cells and tissues [48, 51–55].

Third, the active surface tension gradient and surface strain are dependent upon the size (volume) of the aggregate. The measured volume-dependence of the aggregate surface tension is consistent with the increased phosphorylation of myosin molecular motors at the surface (Supplementary Figure 7). In the absence of actomyosin activity, this size dependence is lost, consistent with the constant surface tension observed in passive systems, such as liquid droplets. Similar size dependence is seen in other systems, for example, in the actomyosin-driven compaction of mesenchymal stem cell volume [56, 57] or the actomyosin assembly for purse string in epithelial sheets [58]. Here, the volume-dependence yields a range of stresses and strains, and thus allows us to relate the two directly and define an active, effective surface modulus.

Finally, Marangoni flows observed in passive fluids are driven exclusively by surface tension gradients. Here, activity contributes to surface stresses, but may also contribute to bulk stresses and the accumulation of pressure within the aggregate. As a result, the elevation of surface tension by internal pressure (e.g. hoop stress) cannot be excluded. Therefore, to be inclusive of this possibility, we term the observed phenomenon presented here 'Marangoni-like' motion.

In summary, cell aggregates, as models of simple tissue have solid-like material properties, which can drive rapid and correlated internal cell motions.

ACKNOWLEDGMENTS

We acknowledge funding ARO MURI W911NF-14-1-0403 to MM and VY as well as NIH RO1 GM126256 to MM and NIH U54 CA209992 to MM and MSY. MM also acknowledge support from Human Frontiers Science Program (HFSP) grant # RGY0073/2018. Any opinion, findings, and conclusions or recommendations expressed in this material are those of the authors(s) and do not necessarily reflect the views of the NSF, NIH, or HFSP. We would like to thank Prof. Erdem Karatekin for help with micropipette measurements. We would also like to thank Prof. Kate Jensen, Dr. Karine Guevorkian, and Prof. Francoise Brochard-Wyart for constructive discussion.

[1] J. Thomson, On certain curious motions observable at the surfaces of wine and other alcoholic liquors, The London, Edinburgh, and Dublin Philosophical Magazine and Journal of Science **10**, 330 (1855).
[2] D. C. Venerusand D. Nieto Simavilla, Tears of wine: new insights on an old phenomenon, Scientific Reports **5**, 16162 (2015).
[3] V. Levich, *Physicochemical hydrodynamics* (Prentice-Hall, Englewood Cliffs, N.J., 1962).
[4] R. Sarmaand P. K. Mondal, Marangoni instability in a viscoelastic binary film with cross-diffusive effect, Journal of Fluid Mechanics **910**, A30 (2021).
[5] N. Bassouand Y. Rharbi, Role of benardmarangoni instabilities during solvent evaporation in polymer surface corrugations, Langmuir **25**, 624 (2009).
[6] E. Bormashenko, S. Balter, R. Pogreb, Y. Bormashenko, O. Gendelman, and D. Aurbach, On the mechanism of patterning in rapidly evaporated polymer solutions: Is temperature-gradient-driven marangoni instability responsible for the large-scale patterning?, Journal of Colloid and Interface Science **343**, 602 (2010).
[7] R. W. Style, A. Jagota, C.-Y. Hui, and E. R. Dufresne, Elastocapillarity: Surface tension and the mechanics of soft solids, Annual Review of Condensed Matter Physics

8, 99 (2017).
[8] H. Delanoë-Ayari, J. P. Rieu, and M. Sano, 4D traction force microscopy reveals asymmetric cortical forces in migrating dictyostelium cells, Phys. Rev. Lett. **105**, 248103 (2010).
[9] M. P. Murrell, R. Voituriez, J.-F. Joanny, P. Nassoy, C. Sykes, and M. L. Gardel, Liposome adhesion generates traction stress, Nat Phys **10**, 163 (2014).
[10] M. Murrell, P. W. Oakes, M. Lenz, and M. L. Gardel, Forcing cells into shape: the mechanics of actomyosin contractility, Nature Reviews Molecular Cell Biology **16**, 486 (2015).
[11] M. Das, C. F. Schmidt, and M. Murrell, Introduction to active matter, Soft Matter **16**, 7185 (2020).
[12] A. B. Kolomeiskyand M. E. Fisher, Molecular motors: A theorist's perspective, Annual Review of Physical Chemistry **58**, 675 (2007).
[13] M. Delarue, J. F. Joanny, F. Julicher, and J. Prost, Stress distributions and cell flows in a growing cell aggregate, Interface Focus **4**, 10.1098/rsfs.2014.0033 (2014).
[14] T. Stylianopoulos, J. D. Martin, V. P. Chauhan, S. R. Jain, B. Diop-Frimpong, N. Bardeesy, B. L. Smith, C. R. Ferrone, F. J. Hornicek, Y. Boucher, L. L. Munn, and R. K. Jain, Causes, consequences, and remedies for growth-induced solid stress in murine and human tumors, Proceedings of the National Academy of Sciences **109**, 15101 (2012), https://www.pnas.org/content/109/38/15101.full.pdf.
[15] T. Colin, G. Dechristé, J. Fehrenbach, L. Guillaume, V. Lobjois, and C. Poignard, Experimental estimation of stored stress within spherical microtissues, Journal of Mathematical Biology **77**, 1073 (2018).
[16] P. Chugh, A. G. Clark, M. B. Smith, D. A. D. Cassani, K. Dierkes, A. Ragab, P. P. Roux, G. Charras, G. Salbreux, and E. K. Paluch, Actin cortex architecture regulates cell surface tension, Nature Cell Biology **19**, 689 (2017).
[17] G. Forgacs, R. A. Foty, Y. Shafrir, and M. S. Steinberg, Viscoelastic properties of living embryonic tissues: a quantitative study, Biophysical Journal **74**, 2227 (1998).
[18] W. M. McFadden, P. M. McCall, M. L. Gardel, and E. M. Munro, Filament turnover tunes both force generation and dissipation to control long-range flows in a model actomyosin cortex, PLOS Computational Biology **13**, 1 (2017).
[19] M. L. Manning, R. A. Foty, M. S. Steinberg, and E.-M. Schoetz, Coaction of intercellular adhesion and cortical tension specifies tissue surface tension, Proceedings of the National Academy of Sciences **107**, 12517 (2010).
[20] K. Guevorkian, D. Gonzalez-Rodriguez, C. Carlier, S. Dufour, and F. Brochard-Wyart, Mechanosensitive shivering of model tissues under controlled aspiration, Proceedings of the National Academy of Sciences of the United States of America **108**, 13387 (2011).
[21] M. E. Dolega, M. Delarue, F. Ingremeau, J. Prost, A. Delon, and G. Cappello, Cell-like pressure sensors reveal increase of mechanical stress towards the core of multicellular spheroids under compression, Nature Communications **8**, 14056 (2017).
[22] M. Delarue, F. Montel, O. Caen, J. Elgeti, J. M. Siaugue, D. Vignjevic, J. Prost, J. F. Joanny, and G. Cappello, Mechanical control of cell flow in multicellular spheroids, Physical Review Letters **110**, 10.1103/PhysRevLett.110.138103 (2013).
[23] F. Montel, M. Delarue, J. Elgeti, L. Malaquin, M. Basan, T. Risler, B. Cabane, D. Vignjevic, J. Prost, G. Cappello, and J. F. Joanny, Stress clamp experiments on multicellular tumor spheroids, Physical Review Letters **107**, 10.1103/PhysRevLett.107.188102 (2011).
[24] F. Montel, M. Delarue, J. Elgeti, D. Vignjevic, G. Cappello, and J. Prost, Isotropic stress reduces cell proliferation in tumor spheroids, New Journal of Physics **14**, 10.1088/1367-2630/14/5/055008 (2012).
[25] G. Cappello, F. Montel, M. Delarue, J. Prost, J. F. Joanny, J. Elgeti, and D. Vignjevic, Mechanical pressure arrests the growth of tumor spheroids, Biophysical Journal **104**, 492a (2013).
[26] K. V. Iyer, R. Piscitello-Gómez, J. Paijmans, F. Jülicher, and S. Eaton, Epithelial viscoelasticity is regulated by mechanosensitive E-cadherin turnover, Current Biology **29**, 578 (2019).
[27] N. Bain, A. Jagota, K. Smith-Mannschott, S. Heyden, R. W. Style, and E. R. Dufresne, Surface tension and the strain-dependent topography of soft solids, Annual Review of Condensed Matter Physics **8**, 99 (2017).
[28] C. Y. Sargent, G. Y. Berguig, M. A. Kinney, L. A. Hiatt, R. L. Carpenedo, R. E. Berson, and T. C. McDevitt, Hydrodynamic modulation of embryonic stem cell differentiation by rotary orbital suspension culture, Biotechnology and Bioengineering **105**, 611 (2010), https://onlinelibrary.wiley.com/doi/pdf/10.1002/bit.22578.
[29] See supplemental material at — for additional data and methodology description, NA.
[30] R. Singh, E. Tjhung, and M. E. Cates, Self-propulsion of active droplets without liquid-crystalline order, Phys. Rev. Research **2**, 032024 (2020).
[31] M. Schmittand H. Stark, Marangoni flow at droplet interfaces: Three-dimensional solution and applications, Physics of Fluids **28**, 012106 (2016).
[32] K. Guevorkian, M. J. Colbert, M. Durth, S. Dufour, and F. Brochard-Wyart, Aspiration of biological viscoelastic drops, Physical Review Letters **104**, 10.1103/PhysRevLett.104.218101 (2010).
[33] P.-G. de Gennes, F. Brochard-Wyart, and D. Querena, *Capillarity and Wetting Phenomena- Drops, Bubbles, Pearls, Waves* (Springer-Verlag New York, New York, 2004).
[34] D. Gonzalez-Rodriguez, K. Guevorkian, S. Douezan, and F. Brochard-Wyart, Soft matter models of developing tissues and tumors, Science **338**, 910 (2012).
[35] S. Douezan, K. Guevorkian, R. Naouar, S. Dufour, D. Cuvelier, and F. Brochard-Wyart, Spreading dynamics and wetting transition of cellular aggregates, Proceedings of the National Academy of Sciences **108**, 7315 (2011).
[36] S. Douezan, J. Dumond, and F. Brochard-Wyart, Wetting transitions of cellular aggregates induced by substrate rigidity, Soft Matter **8**, 4578 (2012).
[37] G. Beaune, C. Blanch-Mercader, S. Douezan, J. Dumond, D. Gonzalez-Rodriguez, D. Cuvelier, T. Ondarçuhu, P. Sens, S. Dufour, M. P. Murrell, and F. Brochard-Wyart, Spontaneous migration of cellular aggregates from giant keratocytes to running spheroids, Proceedings of the National Academy of Sciences **115**, 12926 (2018).
[38] G. Beaune, T. V. Stirbat, N. Khalifat, O. Cochet-Escartin, S. Garcia, V. V. Gurchenkov, M. P. Murrell, S. Dufour, D. Cuvelier, and F. Brochard-Wyart, How cells flow in the spreading of cellular aggregates, Pro-

ceedings of the National Academy of Sciences **111**, 8055 (2014).

[39] M. Kovács, J. Tóth, C. Hetényi, A. Málnási-Csizmadia, and J. R. Sellers, Mechanism of blebbistatin inhibition of myosin ii*, Journal of Biological Chemistry **279**, 35557 (2004).

[40] A. Testa, M. Dindo, A. A. Rebane, B. Nasouri, R. W. Style, R. Golestanian, E. R. Dufresne, and P. Laurino, Sustained enzymatic activity and flow in crowded protein droplets, Nature Communications **12**, 6293 (2021).

[41] M. S. Yousafzai, V. Yadav, S. Amiri, Y. Errami, S. Amiri, and M. Murrell, Active regulation of pressure and volume defines an energetic constraint on the size of cell aggregates, Phys. Rev. Lett. **128**, 048103 (2022).

[42] Q. Xu, K. E. Jensen, R. Boltyanskiy, R. Sarfati, R. W. Style, and E. R. Dufresne, Direct measurement of strain-dependent solid surface stress, Nature Communications **8**, 555 (2017).

[43] Q. Xu, R. W. Style, and E. R. Dufresne, Surface elastic constants of a soft solid, Soft Matter **14**, 916 (2018).

[44] S. Heyden, N. Bain, Q. Xu, R. W. Style, and E. R. Dufresne, Contact lines on stretched soft solids: modelling anisotropic surface stresses, Proceedings of the Royal Society A: Mathematical, Physical and Engineering Sciences **477**, 20200673 (2021).

[45] Z. Shi, Z. T. Graber, T. Baumgart, H. A. Stone, and A. E. Cohen, Cell membranes resist flow, Cell **175**, 1769 (2018).

[46] M. S. Steinberg, On the mechanism of tissue reconstruction by dissociated cells, i. population kinetics, differential adhesiveness, and the absence of directed migration, Proceedings of the National Academy of Sciences **48**, 1577 (1962), https://www.pnas.org/content/48/9/1577.full.pdf.

[47] J. F. Palierne, Linear rheology of viscoelastic emulsions with interfacial tension, Rheologica Acta **29**, 204 (1990).

[48] R. A. Brown, R. Prajapati, D. A. McGrouther, I. V. Yannas, and M. Eastwood, Tensional homeostasis in dermal fibroblasts: Mechanical responses to mechanical loading in three-dimensional substrates, Journal of Cellular Physiology **175**, 323 (1998).

[49] K. Webster, W. Ng, and D. Fletcher, Tensional homeostasis in single fibroblasts, Biophysical Journal **107**, 146 (2014).

[50] M. Basan, T. Risler, J. Joanny, X. Sastre-Garau, and J. Prost, Homeostatic competition drives tumor growth and metastasis nucleation, HFSP Journal **3**, 265 (2009).

[51] P. W. Oakes, Y. Beckham, J. Stricker, and M. L. Gardel, Tension is required but not sufficient for focal adhesion maturation without a stress fiber template, Journal of Cell Biology **196**, 363 (2012).

[52] V. Ajeti, A. P. Tabatabai, A. J. Fleszar, M. F. Staddon, D. S. Seara, C. Suarez, M. S. Yousafzai, D. Bi, D. R. Kovar, S. Banerjee, and M. P. Murrell, Wound healing coordinates actin architectures to regulate mechanical work, Nature Physics **15**, 696 (2019).

[53] M. S. Yousafzai, V. Yadav, S. Amiri, M. Staddon, A. P. Tabatabai, Y. Errami, G. Jaspard, S. Amiri, S. Banerjee, and M. Murrell, Tissue pressure and cell traction compensate to drive robust aggregate spreading, bioRxiv –, (2020).

[54] M. F. Staddon, D. Bi, A. P. Tabatabai, V. Ajeti, M. P. Murrell, and S. Banerjee, Cooperation of dual modes of cell motility promotes epithelial stress relaxation to accelerate wound healing, PLOS Computational Biology **14**, 1 (2018).

[55] J. D. Humphrey, Vascular adaptation and mechanical homeostasis at tissue, cellular, and sub-cellular levels, Cell Biochemistry and Biophysics **50**, 53 (2008).

[56] B. M. Bijonowski, S. I. Daraiseh, X. Yuan, and T. Ma, Size-dependent cortical compaction induces metabolic adaptation in mesenchymal stem cell aggregates, Tissue Engineering Part A **25**, 575 (2019), pMID: 30187829, https://doi.org/10.1089/ten.tea.2018.0155.

[57] K. C. Murphy, B. P. Hung, S. Browne-Bourne, D. Zhou, J. Yeung, D. C. Genetos, and J. K. Leach, Measurement of oxygen tension within mesenchymal stem cell spheroids, Journal of The Royal Society Interface **14**, 20160851 (2017).

[58] Y. Danjoand I. Gipson, Actin 'purse string' filaments are anchored by E-cadherin-mediated adherens junctions at the leading edge of the epithelial wound, providing coordinated cell movement, Journal of Cell Science **111**, 3323 (1998).